Experimental review of theoretical predictions on the Compton effect

Özgen Tunç Türker, Thibault Barnouin and Livio Redard-Jacot

26/02/2021

Abstract

The theoretical prediction for the Compton scattering are tested experimentally. The setup consists of three detectors selecting 511 keV photons and measuring the rate and energy of photons and electrons that interact via Compton scattering. The data flow is substantially reduced by online data analysing. The results of the energy measurement and the differential cross section are in agreement with the theoretical prediction.

1 Introduction

The observation of the Compton effect was a milestone in the validation of the quantum theory and the quantization of electromagnetic waves. Opposite to the classical prediction, one observes that the scattering of an incident photon with an electron leads to an increased photon wavelength depending on the scattering angle θ. By treating the radiation as a stream of photons with each a momentum h/λ, the energy of the scattered photon can be derived as:

$$E_{\gamma'} = \frac{E_\gamma}{1 + \frac{E_\gamma}{m_0 c^2}(1 - cos\theta)} \quad (1)$$

where m_0 is the electron rest mass and E_γ the initial energy of the photon.

The differential cross section for this scattering process is predicted by quantum electrodynamics in the form of the Klein-Nishina formula:

$$\frac{d\sigma}{d\Omega} = \frac{r_e^2}{2} \frac{1}{(1+\alpha(1-cos\theta))^2} \left(1 + cos^2\theta + \frac{\alpha^2(1-cos\theta)^2}{1+\alpha(1-cos\theta)}\right) \quad (2)$$

where r_e is the classical electron radius and $\alpha = E_\gamma/m_0c^2$.

In this paper, an experimental setup is proposed to test the theoretical predictions for the Compton effect.

2 Experimental Setup

Two Teledyne Isotopes NaI(Tl) scintillation detectors and one ORTEC 905-3 NaI(Tl) scintillation detector are used in the experiment. Electronic modules implemented are all ORTEC models, namely: 556 High Voltage Power Supply, 460 Delay Line Amplifier, 551 Timing Single Channel Analyzer, 414A Fast Coincidence and 871 Timer and Counter. Moreover, a FASTER multichannel analyser is used in the experiment.

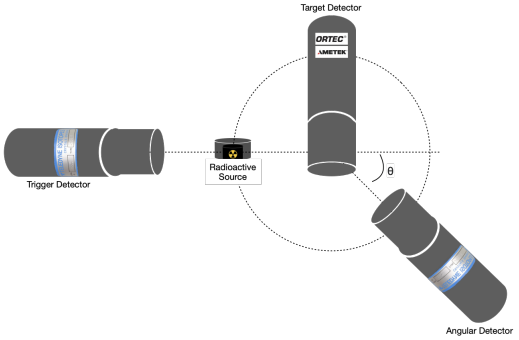

Figure 1: Configuration of the detectors

2.1 Design

As shown in the configuration of the detectors in Fig. 1, three detectors are used at the same time. The design is based on working with the 511 keV photons produced in the β^+ decay of ^{22}Na [1]. Because the positron originating from the decay annihilates to two photons which are back-to-back, the source, the "trigger" and the "target" detectors are placed in a line, with the source in-between. The "trigger" detector catches one photon as its pair goes through the experimental setup and deposits part of its energy in "target" detector, as it is seen in Fig. 1. The third detector, called "angular", is aimed to capture the photons scattered in the "target" via Compton Effect. This third detector is placed on a rail system that can move it on the circle seen in Fig. 1 to detect scattered photon at different angles in each acquisition. In this configuration the flight time of the photons are neglected in respect to the detectors scintillation time ($\sim 230ns$ [2]). This assumption is used to put all three detectors in coincidence. Having a coincidence in all detectors increases the probability that the recorded event is the Compton scattering event of the 511 keV photon. In the target the energy of the recoil electron,

the other product of the Compton scattering, can be read out.

2.2 Test of devices

Before moving to the final setup configuration, all of the used modules are tested.

First, the energy resolutions for different voltages are computed for the 662 keV full absorption peak of the ^{137}Cs by using eq. 3.

$$R = \sigma\sqrt{2\ln 2}/N_{\text{channel}} \tag{3}$$

where σ is the standard deviation of the 662 keV peak and N_{channel} is the number of the channel [3].

The voltage-resolution plots are obtained for all three detectors, the stability plateau is verified and the value in the middle is taken as a working voltage for each detector (see table 1).

To set the gains for each 460 Delay Line Amplifier, a "calibration setup" is built. This setup consists of only one detector that is connected to the amplifier and powered by high voltage. The amplifier is connected to the FASTER multichannel analyzer. The Spectra of different sources such as ^{22}Na, ^{137}Cs, ^{60}Co and ^{152}Eu are observed by the computer which is connected to the FASTER and the gain of the each module 460 is changed to see the each same peaks in the spectrum by all of the 3 detectors.

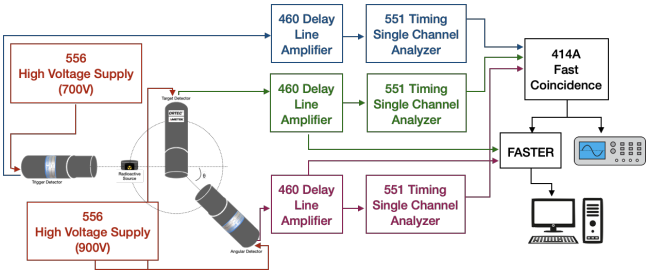

Figure 2: Experimental Setup

Moreover, in order to reduce data flow, online data reduction is realised by the 551 Timing Single Channel Analyser (TSCA). It is implemented to the setup after the amplifier. The FASTER card is used to selecting the energy window used. Because 511 keV photons are considered, the energy window is selected in the range from 0 to 511 keV. The ^{22}Na spectrum is seen with each detector and minimum and maximum voltage limits are set for each detector's 551 TSCA. This operation is done by triggering the analog signal on the FASTER with the logic signal of 551 module.

Finally, the coincidence of the detectors are checked by pairs of trigger-target and trigger-angular. The delay of the trigger detector path is set to 0.00μs and the delay on the other path is increased by steps. Coincidence events are counted by the ORTEC module 871 Timer and Counter. The coincidence plateau is verified and the value at the middle of the plateau is set as delay for the target or respectively the angular detector (see in the table 1).

	Trigger	Target	Angular
Voltage [V]	900	700	900
Gain (460)	$50 + 0.75$	$20 + 0.85$	$100 + 0.81$
V_{max} [V] (551)	8.80	5.92	6.70
V_{min} [V] (551)	6.94	0.00	0.00
Delay [μs](551)	0.00	1.65	2.78

Table 1: Setup parameters for all 3 detectors

By following all these processes, all the parameters for the electronic modules are obtained as given in table 1 and the final experimental setup with all modules is built as depicted in Fig. 2.

2.3 Energy Calibration

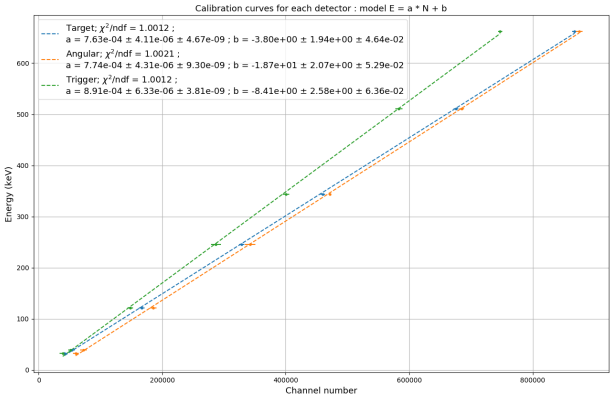

Figure 3: Calibration curves for the three detectors

Using seven characteristic peaks in the decay spectra of ^{152}Eu, ^{22}Na and ^{137}Cs between 32 – 662 keV, a linear relation between the number of channels and the energy is obtained. Fig. 3 shows the linear fit, the calculated χ^2, as well as the error bars on the values. The errors on the fit were re-scaled to get a χ^2 close to one because they underestimated the real error.

2.4 Efficiency of the detectors

To determine the differential cross section, the knowledge of the intrinsic peak efficiency of the detectors as a function of the energy is required. To do so, the number of detected events below a full-absorption peak $N_{detected}$ is compared to number of photons emitted by the source N_{source}. Five peaks are used from the decay spectra of ^{152}Eu , ^{22}Na and ^{137}Cs up to 662 keV. The region of interest lies below 511 keV at the possible energies of the Compton scattered photons. Considering the solid angle of the detector, the

intrinsic peak efficiency is then given by:

$$\epsilon_{int} = \frac{\epsilon_{abs}}{\epsilon_{geo}} = \frac{4\pi}{\Omega}\frac{N_{detected}}{N_{source}} \quad (4)$$

The solid angles of the angular and trigger detector (circular surface) Ω_1 and of the target detector (quadratic surface) Ω_2 are given as follows [4]:

$$\Omega_1 = 2\pi(1 - \frac{d}{\sqrt{d^2+a^2}}),\ \Omega_2 = 4\tan^{-1}(\frac{a^2/2d}{\sqrt{2a^2+4d^2}}) \quad (5)$$

where a is the radius of the detector and d the distance to the source. $N_{detected}$ is obtained by fitting the peak with a Gaussian and a second degree polynomial and using the Gaussian parameters to integrate the events below the peak. N_{source} is calculated as follows:

$$N_{sources} = A \times F \times t \quad (6)$$

where A is the Activity of the source, F is the branching ratio of the β^+ decay of ^{22}Na times the number of photon emitted in this process [1] and t is the time of acquisition.

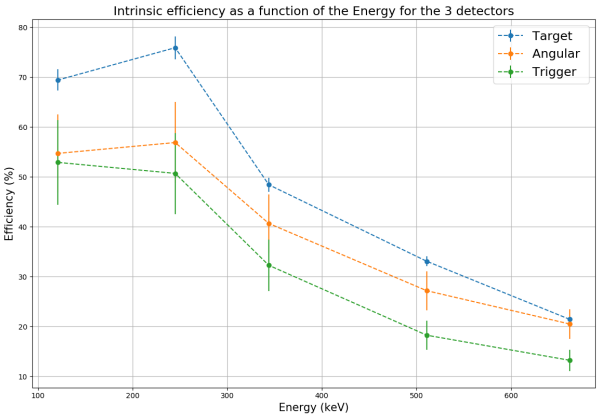

Figure 4: Intrinsic peak efficiency of the three detectors for energies corresponding to peaks in the spectra of ^{152}Eu , ^{22}Na and ^{137}Cs.

Fig. 4 shows the resulting efficiencies of the three detectors. It shows the expected decrease with higher energies due to the decreasing cross section of the photoelectric effect. At low energies, the efficiency is reduced because the energies become comparable to the binding energy of the scintillators electrons. The points are later fitted in log-log scale with a second degree polynomial [5] to obtain the efficiency in the whole region of interest.

3 Results

Having a calibrated Setup that includes effective background reduction, measurements are taken for several angular positions whose results are presented in the following.

3.1 Energy of the scattered photon and electron

The spectrum of the scattered photon (Angular) shows a different characteristics than the spectrum of the electron (Target) as depicted in Fig. 5 for an acquisition at 70°.

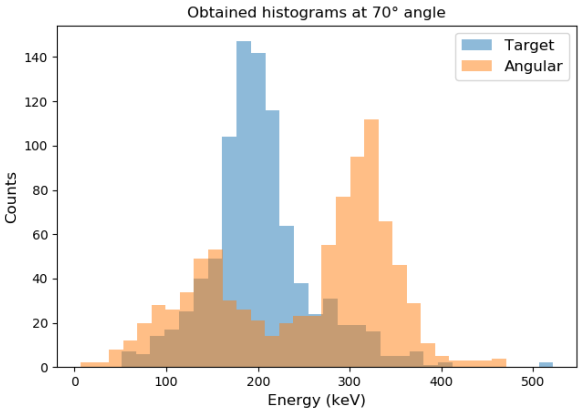

Figure 5: Energy spectra of Target and Angular detectors at a 70° angle.

The photon shows a full absorption peak, that is used in the next section to calculate the cross section, but also a second peak from Compton scattering in the scintillator without full absorption. The energy transferred from the photon to the electron appears as one full absorption peak.

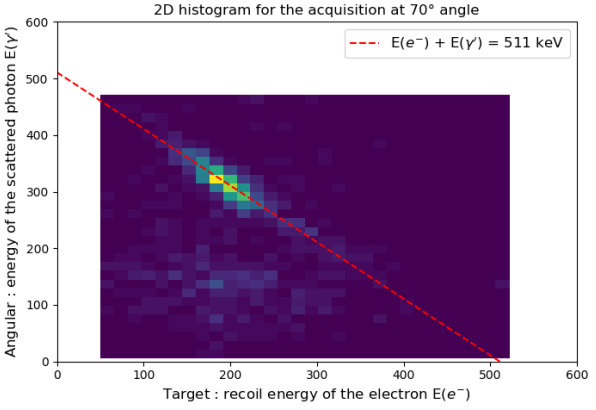

Figure 6: 2d histogram of events in Target and Angular detectors at a 70° angle

Fig. 6 shows a 2d histogram of the two spectra. It illustrates that the energy of the electron and the scattered photon add up to the initial energy of 511 keV (red line) and thereby confirms the energy shift of the photon. Quantitatively, the energies are determined by fitting the full absorption peak, resulting in a summed energy of 510.8 ± 2.4 keV.

3.2 Differential cross section

Fig. 7 shows the results of the differential cross section for six different angular positions in comparison to the theoretical prediction that is given by eq. 2.

They are calculated with the following formula:

$$\left[\frac{d\sigma}{d\Omega}\right]_{\text{measured}} = \frac{N_{detected}}{n_e\, I\, \Delta\Omega\, t\, \epsilon_1\, \epsilon_3} \frac{\Omega_{trigger}}{\Omega_{target}} \tag{7}$$

where n_e is the number of electrons in the target, I is the incident photon flux, $\Delta\Omega$ is the finite solid angle of the angular detector, t is the acquisition time and ϵ_1 and ϵ_3 is the efficiency of the trigger and the angular detector. $N_{detected}$ is obtained in the same way as in Sec. 2.4. The ratio of the solid angles takes into account that the trigger covers a smaller solid angle than the target. At the bottom of Fig. 7, it is shown that the measurements are in agreement with the theory.

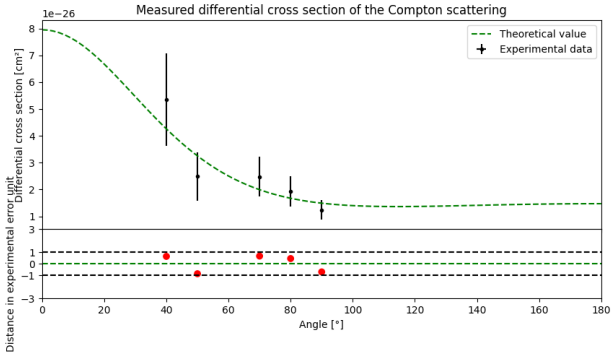

Figure 7: Comparison of the measured differential cross sections to the theoretical prediction.

4 Discussion

In this section the limitations of our experimental setup and the sources of errors are discussed.

A few errors comes directly from the experimental setup itself. The uncertainty on the distances will be of most importance when computing geometrical parameters such as the solid angles of our detectors. Given our tools, this repeated measurement uncertainty has been assessed to 2 mm (and 0.5 mm for the documented crystal length of the ORTEC detector [2]), it can be improved with better suited instrumentation. The electronics stability can be a source of errors as an energy window drift was witnessed on the trigger detector TSCA module over the two weeks of acquisition. This has been taken into account by estimating again the errors. Thanks to the input voltage calibration on a resolution stability plateau, our setup is such that we can neglect any other instability.

The use of an online Fast Coincidence module to trigger our acquisition asks the question of its efficiency and stability. The efficiency was found to be $\sim 100\%$ and stable in time.

In this setup the extension of the angular detector make the acquisition for a range of angles of size $\Delta\theta \approx \frac{r_2}{d_{\text{target}}}$. Given the photon energy dependence on the scattering angle (see eq. 1) a relative error is computed on the energy with eq. 8:

$$\frac{\Delta E}{E}(\theta) = \left|\frac{\sin\theta}{2-\cos\theta}\right| \cdot \Delta\theta \tag{8}$$

The Errors from the data analysis come in 2 types: statistical and systematical errors.
Statistical errors come from the number of events on which the analysis is performed. As our setup has a low data flow and requires long acquisition, these errors are quite important in our analysis. This can be reduced with longer acquisition times that could not be met in our short time at the lab.
Systematic errors come from the fitting of models on our experimental data. Thanks to clean acquisitions with this setup (low noise and background) our data was well fitted by Gaussian with polynomial background models, resulting in small systematic errors.

References

[1] Marie-Martine Bé, Vanessa Chisté, Christophe Dulieu, Xavier Mougeot, Edgardo Browne, Valery Chechev, Nikolay Kuzmenko, Filip Kondev, Aurelian Luca, Monica Galan, et al. Table of radionuclides (vol. 5–a= 22 to 244). *Monographie BIPM-5*, 5, 2010.

[2] ORTEC-AMETEK. 905 Series NaI(Tl) Scintillation Detectors. `https://www.ortec-online.com/products/radiation-detectors/scintillation-detectors/scintillation-detector-types/905-series`.

[3] Glenn F Knoll. *Radiation detection and measurement*. John Wiley & Sons, 2010.

[4] Richard J Mathar. Solid angle of a rectangular plate. *Max-Planck Institute of Astronomy*, pages 1–9, 2015.

[5] Marie-Christine Lépy. Detection efficiency. *Laboratoire National Henri Becquerel, CEA Saclay, F-91191 Gif-sur-Yvette cedex, France, IAEA-ALMERA Technical Visit*, 2010.